Materials and Design 170 (2019) 107689

Contents lists available at ScienceDirect

Materials and Design

journal homepage: www.elsevier.com/locate/matdes

3D printing of hybrid MoS_2-graphene aerogels as highly porous electrode materials for sodium ion battery anodes

Emery Brown [a], Pengli Yan [b], Halil Tekik [b], Ayyappan Elangovan [a], Jian Wang [c], Dong Lin [b,*], Jun Li [a,*]

[a] Department of Chemistry, Kansas State University, Manhattan, KS 66506, USA
[b] Department of Industrial and Manufacturing Systems Engineering, Kansas State University, Manhattan, KS 66506, USA
[c] Department of Mechanical and Materials Engineering, University of Nebraska-Lincoln, Lincoln, NE 68588, USA

HIGHLIGHTS

- MoS_2-reduced graphene oxide aerogels have been firstly printed with a three-dimensional freeze printing method.
- The hybrid structure consists of small MoS_2 patches attached on larger two-dimensional rGO flakes in a macroporous framework.
- The hybrid aerogels are utilized for sodium ion battery anodes.

GRAPHICAL ABSTRACT

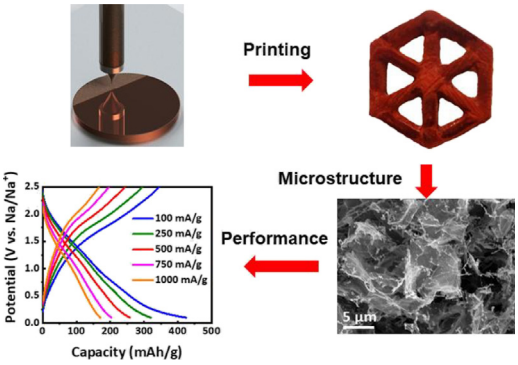

ARTICLE INFO

Article history:
Received 23 December 2018
Received in revised form 3 March 2019
Accepted 4 March 2019
Available online 5 March 2019

Keywords:
3D printing
Hybrid MoS_2/graphene aerogel
Freeze-casting
Sodium ion battery
Porous electrode materials

ABSTRACT

This study reports a 3D freeze-printing method that integrates inkjet printing and freeze casting to control both the microstructure and macroporosity via formation of ice microcrystals during printing. A viscous aqueous ink consisting of a molecular MoS_2 precursor (ammonium thiomolybdate) mixed with graphene oxide (GO) nanosheets is used in the printing process. Post-treatments by freeze-drying and reductive thermal annealing convert the printed intermediate mixture into a hybrid structure consisting of MoS_2 nanoparticles anchored on the surface of 2D rGO nanosheets in a macroporous framework, which is fully characterized with FESEM, TEM, XRD, Raman spectroscopy and TGA. The resulting hybrid MoS_2-rGO aerogels are studied as anodes for sodium ion batteries. They present a high initial specific capacity over 429 mAh/g at C/3.3 rate in the potential range of 2.5–0.10 V (vs Na^+/Na). The process involves both reversible 2 Na^+ insertion and slow irreversible conversion of MoS_2 to metallic Mo. At higher rates, the conversion reaction is suppressed and the electrode is dominated by fast Na^+ intercalation with good stability. This demonstrates that the 3D printing technology can be used as a processing technique to control the materials properties for energy storage.

1. Introduction

3D printing, a technique for rapid prototyping of materials, architecture, and systems, has recently been applied for the fabrication of Li-ion battery (LIB) electrodes in interdigitated microarchitectures with a

* Corresponding authors.
E-mail addresses: dongl@ksu.edu (D. Lin), junli@ksu.edu (J. Li).

https://doi.org/10.1016/j.matdes.2019.107689

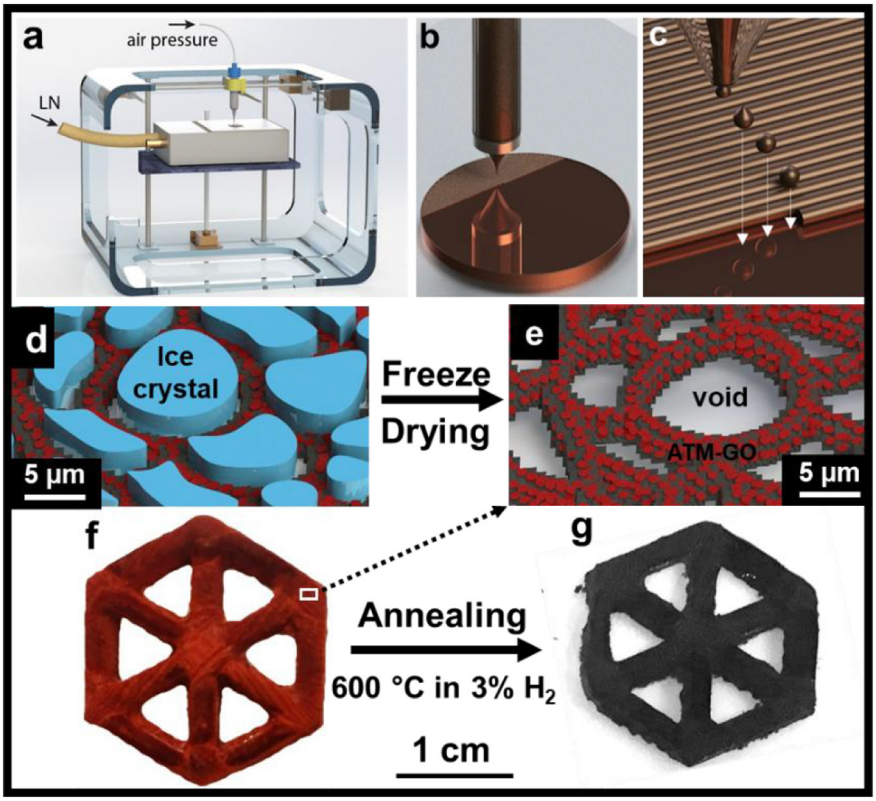

Fig. 1. Schematics of the 3D "drop-on-demand" ink jet printing setup (a), the printing process of the ATM-GO droplets in a raster fashion (b–c), ice template formation (d) during printing, and the resulting ATM-GO aerogel after freeze drying (e). An example macrostructure of the 3D printed ATM-GO aerogel after free-drying (f) and the resulting MoS_2-rGO aerogel after reductive thermal annealing (g) are shown. (For interpretation of the references to color in this figure, the reader is referred to the web version of this article.)

printed feature size around 100 μm [1,2]. While these studies demonstrate the potential of 3D printing for future personal design of energy storage devices, they have mainly focused on a proof-of-concept using well established electrode materials such as the lithium iron phosphate (LFP) and lithium titanium oxide (LTO). The theoretical specific capacity of these materials is relatively low, being 170 mAh/g for LFP and 174 mAh/g for LTO. Thus, it was not challenging to maintain the integrity of the 3D printed structures during charge-discharge cycles due to the relatively small volume changes (<5%). Other studies have explored the 3D printing process for rapid prototyping of freestanding disk electrodes for LIB coin cells [3] or improving Li^+ ion transport in electrodes by printing $LiMn_{1-x}Fe_xPO_4$ nanocrystal inks into parallel lines [4].

Another direction in 3D printing research is to utilize the layer-by-layer additive technology as a materials processing tool to control the internal micro-/nano- structures of the printed materials in desired macrostructures. A recent study by Rocha et al. [5] demonstrated the successful printing of woodpile and interdigitated structures using chemically modified graphene (CMG) ink interfaced with the current collectors printed with a copper colloid ink. The printed precursors were subject to freeze-drying and thermal treatment to form reduced CMG flakes. The materials not only retained the original 3D printed macro-architecture but also formed a highly porous internal structure with interconnected pores on the order of ~5 μm. Moreover, the high electrical conductivity and large surface area of the reduced CMG flakes led to relatively high-powered electrochemical supercapacitors [5]. In principle, this method can be applied on fabricating advanced secondary batteries by incorporating proper energy storage materials. In this work, we use a further improved 3D freeze-printing (3DFP) method as a novel materials processing technique to prepare highly porous MoS_2/graphene hybrid aerogels as the anode for more challenging future sodium ion batteries (SIBs). Such interconnected porous structures are critical in mitigating the stress induced by the larger volume changes during charge-discharge cycles than that in the previous LIB studies due to the combination of higher specific capacity (over 300 mAh/g) and larger ion size (0.102 nm for Na^+ vs 0.076 nm for Li) [6,7].

Graphene and molybdenum disulfide (MoS_2) belong to a broad family of two-dimensional (2D) layered materials which have been widely investigated due to their exceptional properties [8]. For instance, MoS_2 forms a layered structure containing three-atom layers (S-Mo-S) stacked together through *van der Waals* interactions, which facilitates

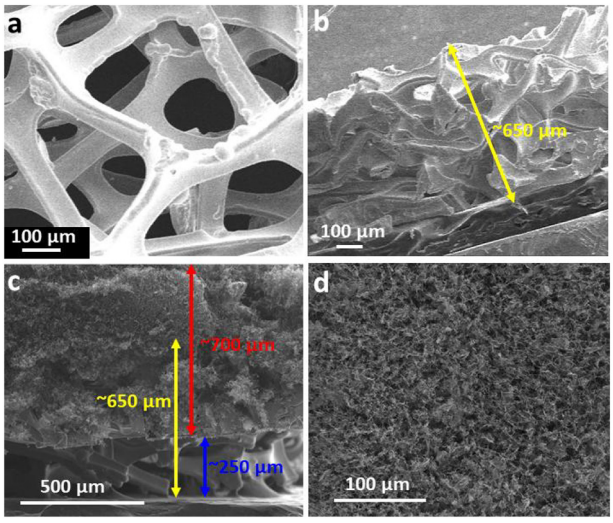

Fig. 2. SEM images of a) top-view and b) cross-sectional view of a compressed Ni form. SEM images c) at the cross-section of MoS_2-rGO aerogel on the nickel foam illustrating the ~700 μm thickness of MoS_2-rGO aerogel that is partially embedded in the ~650 μm thick Ni foam and d) the morphology of the highly porous interconnected network of the MoS_2-rGO aerogel.

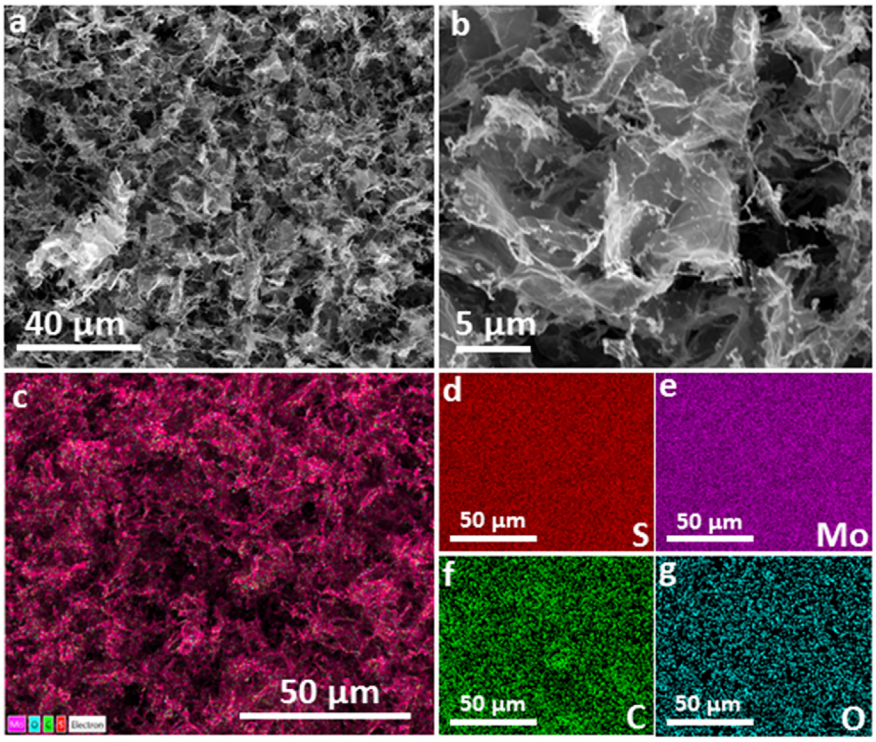

Fig. 3. Low a) and high b) magnification SEM images of MoS_2-rGO printed on a Ni foam. EDS layered elemental mapping of c) all elements, d) sulfur (red), e) molybdenum (purple), f) carbon (green) and g) oxygen (blue). (For interpretation of the references to color in this figure legend, the reader is referred to the web version of this article.)

intercalation of ions. However, it suffers from fast structure deterioration and low electrical conductivity [9,10]. On the other side, graphene is the most promising 2D single atom thick material, especially as a conductive backbone due to its high electrical conductivity, superior flexibility, and excellent chemical resistance [10]. Therefore, hybrid 2D materials, like MoS_2/graphene, have attracted broad attention in order to combine the advantages from both components for applications such as LIBs [9–11], SIBs [12], electromagnetic wave absorber [10], chemical sensor [13], etc. Graphene oxide (GO) is a form of heavily oxidized graphene which can be better dispersed in aqueous solutions making the materials processing much more flexible. For this reason, GO has been included in 3D printing inks to improve the electrical

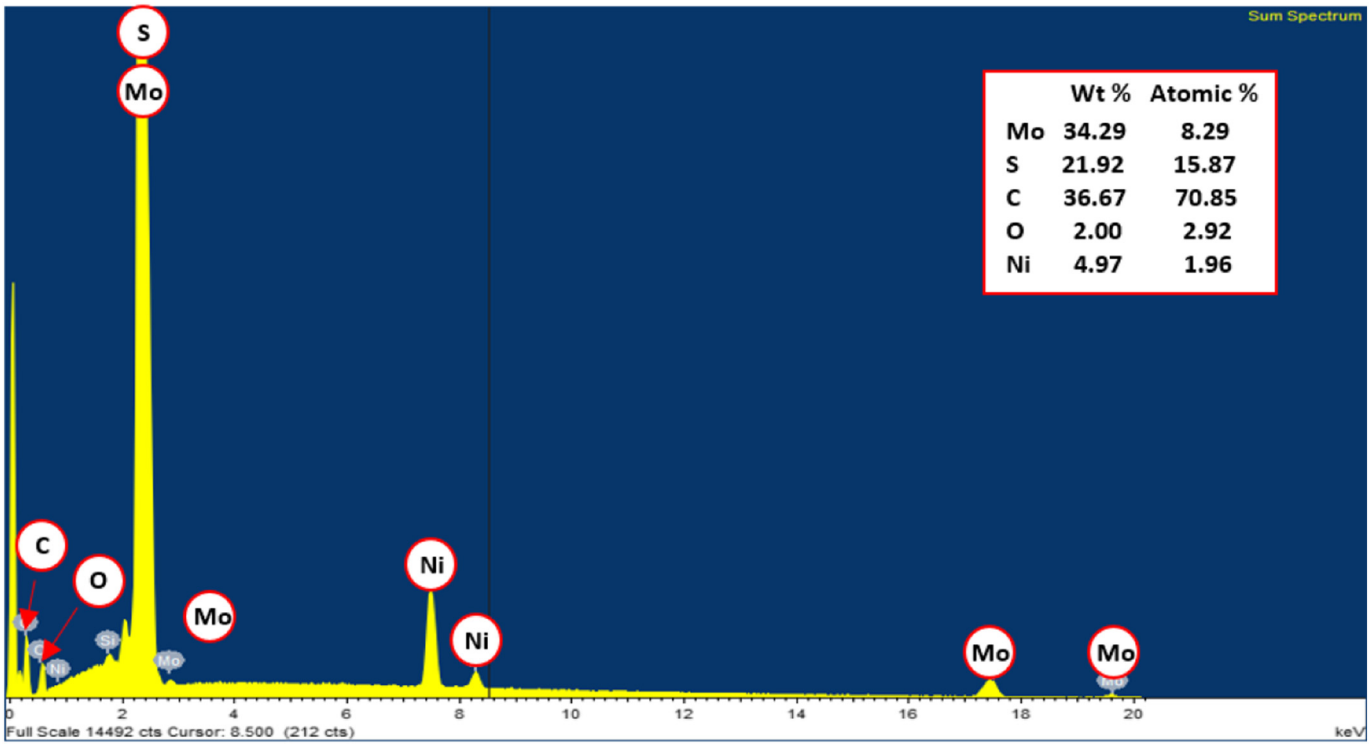

Fig. 4. An EDS spectrum of the MoS_2-rGO aerogel on the nickel foam.

conductivity of the printed electrodes [2,5]. More importantly, GO can be converted into reduced graphene oxide (rGO) through a postdeposition thermal annealing process to remove the oxygenated functional groups and reorganize GO into higher quality graphene [5]. Thus, the electrical conductivity is increased by several orders of magnitude which is essential for high-power energy storage applications.

In this work, we print 3D MoS_2/graphene hybrid aerogel, shown in Fig. 1, as anodes for SIBs using the 3DFP technique developed in our previous study on 3D printing of graphene aerogels [14–17]. The key innovation is employing a cold substrate plate at −30 °C (Fig. 1a) so that the aqueous ink droplets can be rapidly frozen as ice during printing. An aqueous GO-based ink consisting of adjustable concentration of GO nanoflakes and ammonium thiomolybdate (ATM) as the MoS_2 precursor is used in the printing process. The post-printing freeze-drying followed by thermal treatment in Ar gas containing 3% H_2 preserves the porous structure created by ice crystals during 3D printing while converting ATM into MoS_2 by thermal decomposition and thermally reducing GO into rGO. Such printed hybrid aerogels form a continuous highly conductive rGO backbone with the nanoscale MoS_2 sheets attached to the graphene surface serving as the Na^+ intercalation host. The half-cell SIB tests demonstrate that such 3D printed MoS_2/graphene aerogels can achieve a specific capacity close to the theoretical values at low charge-discharge rates and good stability at higher rates. This study demonstrates an innovative method to fabricate hybrid aerogel-based 3D architectures for broad electrical energy storage devices.

2. Results and discussion

The 3D hybrid MoS_2/rGO aerogels were printed by the 3DFP technique, which combines inkjet printing with freeze casting. The schematic of the 3DFP setup is shown in Fig. 1a–c. ATM and GO nanoflakes (300–800 nm in average size) were dispersed in deionized (DI) water and utilized as the precursor ink. To ensure a good interface with the printed material for battery tests, a Ni foam with interconnected ~300 μm diameter pores (Fig. 2a and b) is used as the current collector which was firmly pressed onto a cold plate set at −30 °C. The ATM-GO droplets rapidly froze into ice crystals, as illustrated in Fig. 1d. During this process, the ATM-GO precursors were squeezed between ice crystals to form a continuous matrix. The 3D printed patterns were placed in a freezer set at −70 °C for 24 h to achieve further ice crystal growth and then transferred to a freeze drier to remove the ice template and form an ATM-GO precursor aerogel, as shown in Fig. 1e. The 3D macro architecture can be controlled in any pattern down to 100 μm resolution via the preset 3D printing models. An example is shown in Fig. 1f. In this study, a simple continuous film is used. The precursor aerogel was then thermally annealed in 3% hydrogen (97% argon) for 2 h at 600 °C to produce the MoS_2-rGO hybrid aerogel represented by the characteristic color change from red-brown (Fig. 1f) to black-grey (Fig. 1g). The printed architectures were clearly retained after going through all these processes. To the best of our knowledge, it is the first time to achieve 3D printing of MoS_2-rGO hybrid aerogels.

The microstructures of printed hybrid MoS_2-rGO aerogel were characterized in details. The low-magnification SEM image in Fig. 3a reveals the rather uniform morphology of the MoS_2-rGO aerogel, which comprises of an interconnected network of micron-sized flakes. The high-magnification SEM image in Fig. 3b reveals the presence of 5–10 μm pores among wrinkled rGO flakes (5–10 μm in size) stacked into 100–200 nm thick framework. From the cross-sectional SEM image in Fig. 2c, the thickness of the printed MoS_2-rGO aerogel film is estimated to be ~700 μm, which is partially embedded in the 650 μm thick pressed nickel foam. Such Ni foam with interconnected pores of 200–300 μm is commonly used as the 3D current collector in LIBs. It also plays an important role in this study to regulate the freeze-printing process. It's worth noting that the morphology of the obtained MoS_2-rGO aerogel (Figs. 2d, 3a and b) is quite different from that obtained by traditional 3D printed/freeze-dried materials on planar substrates which consisted of columnar or wall-like structures separated by large voids of ~100–300 μm in size generated by ice crystals [14,18] The open 3D Ni foam framework apparently changed the temperature gradient and eliminated the formation of large columnar ice crystals from surface of the cold plate. The large temperature gradient along a particular direction is known to be the driving force for the freeze casting in previous studies [14,16]. The EDS mapping in Fig. 3c–g shows a homogeneous mixture of carbon, oxygen, molybdenum and sulfur throughout the aerogel (with a representative EDS spectrum in Fig. 4 showing the signal from all four elements).

The microstructure was further characterized by high-resolution TEM. The bright-field TEM image in Fig. 5a shows that the hybrid structure consists of small darker MoS_2 patches attached on larger thin rGO flakes. Further study by high-angle annular dark-field scanning transmission electron microscope (HAADF-STEM) images in Fig. 5b–d show that MoS_2 forms a dense layer consisting of 10 to 50 nm nanoparticles on the surface of much larger rGO flakes. The high-resolution images (Figs. 5e and f) and SAED patterns (insets in Fig. 5e and f) indicate that the MoS_2 nanoparticles are polycrystals and most of them have the hexagonal lattices aligned in the rGO surface plane (as reflected in the dominating six-fold SAED patterns). In contrast, the morphology of the materials produced by 3D printed ATM alone show very different morphologies and random crystal orientations (see Fig. 6). The hybrid structure of MoS_2-rGO consisting of small MoS_2 patches on larger rGO flakes is further illustrated with more TEM images and EDS mapping in Fig. 7.

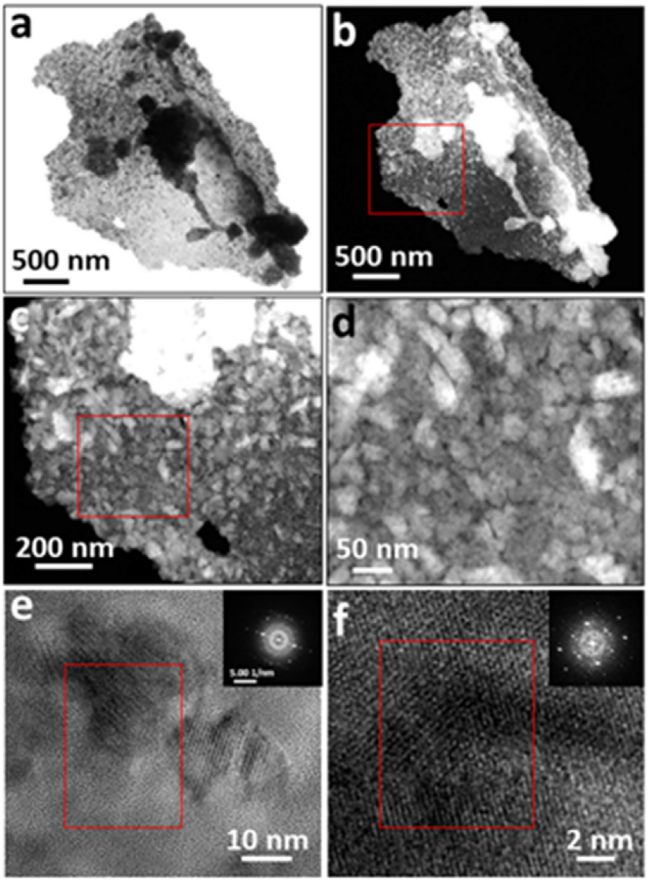

Fig. 5. a) The bright-field TEM image and b)–d) dark-field HAADF-STEM images of a MoS_2-rGO aerogel particle. The red boxes in (b) and (c) indicate the region that the next higher resolution images in panels (c) and (d) were taken. e) and f) HRTEM images of the same aerogel particle including SAED inserts from the region highlighted with the red boxes. (For interpretation of the references to color in this figure legend, the reader is referred to the web version of this article.)

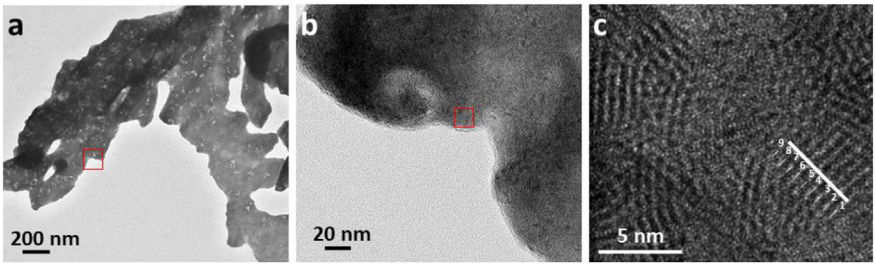

Fig. 6. a) and b) Low-magnification TEM images and c) HRTEM image of bare MoS_2 materials produced with reductive thermal treatment of the 3D printed structure using the ATM precursor alone. A lattice spacing of 0.63 nm corresponding to the interlayer spacing of MoS_2 can be seen in the TEM image in panel c.

The structure and materials properties of the 3D printed MoS_2-rGO aerogels are further characterized with XRD, Raman spectroscopy and thermal gravimetric analyses (TGA). The XRD spectrum in Fig. 8a matches well with the pattern of JCPDS: 37-1492 database. The signature diffraction peak (002) at the 2θ of 14.22° corresponds to a d-spacing of 0.62 nm which is consistent with the HRTEM images of bare MoS_2 in Fig. 6c. The relatively large spacing and weak interlayer interactions are advantageous to the intercalation of sodium ions. It's worth noting that there is no (002) diffraction from rGO layers, suggesting that the commonly encountered issue of rGO restacking was avoided likely due to the high MoS_2 content on rGO surface [19,20]. The Raman spectra in Fig. 8b show the signature peaks of MoS_2 at 379 and 403 cm^{-1} corresponding to the first-order Raman active modes E^1_{2g} and A_{1g}, respectively. These bands originate from the opposite vibration of two S atoms with respect to the Mo atom and the out-plane vibration of S atoms, respectively [21,22]. A smaller peak at 458 cm^{-1} is associated with 2 LA (M) which originates from the second-order zone-edge phonon [23–25]. The two peaks at the Raman shift of 1353.0 and 1600.0 cm^{-1} are associated with the D and G bands of rGO originating from the vibrational modes from sp^3-bonded carbon atoms in amorphous carbon or defect sites and the in-plane vibration of sp^2-bonded carbon atoms, respectively. The ratio of peak intensity of D and G bands is close to 1.0, indicating the relatively large average size of sp^2 domains in the final rGO [26]. In addition, two weak peaks corresponding to 2D and S3 bands are observed at 2676 and 2940 cm^{-1}, respectively. The large intensity ratio of I_{S3}/I_{2D} = ~2.0 in inset of Fig. 8b

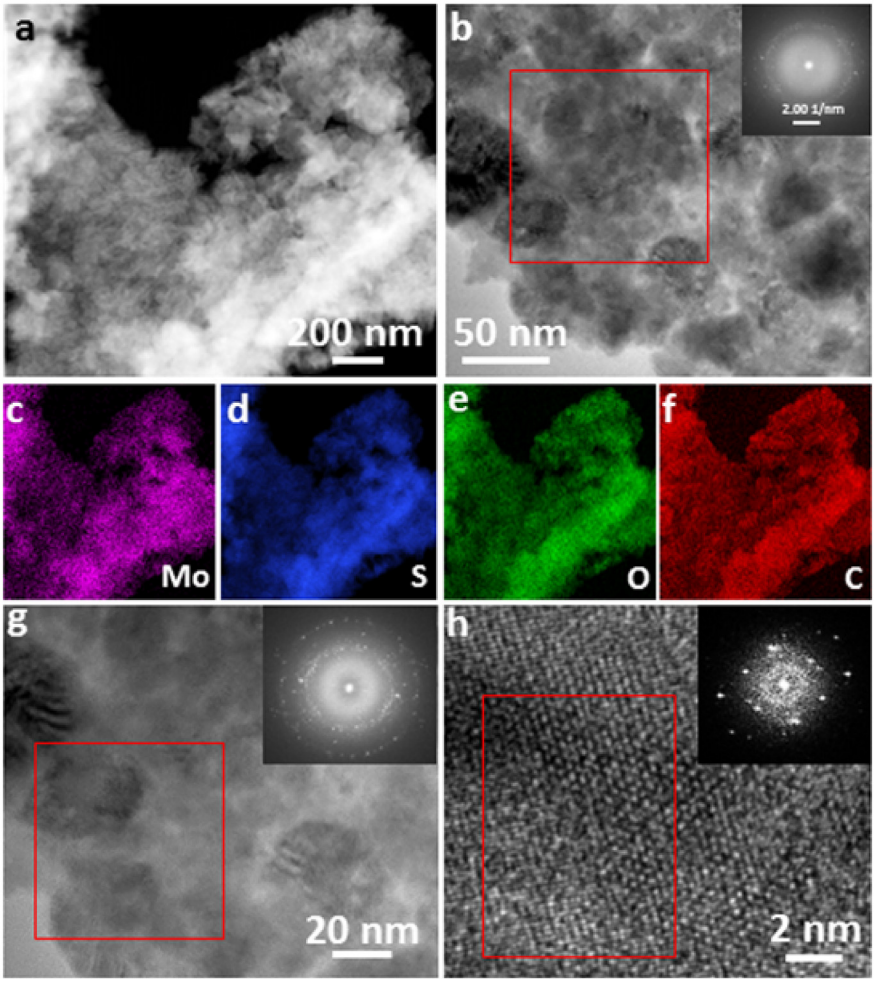

Fig. 7. HAADF-STEM images at a) low and b) high magnifications of a MoS_2-rGO particle. EDS elemental mapping of the STEM image with c) molybdenum (purple), d) sulfur (blue), e) oxygen (green) and f) carbon (red). HRTEM images (g and h) of MoS_2-rGO showing the lattice of MoS_2 and rGO, respectively, with SAED patterns from the red-boxed area shown in the insets. (For interpretation of the references to color in this figure legend, the reader is referred to the web version of this article.)

indicates the presence of a relatively high concentration of defects in the rGO lattice, which may be necessary to obtain a strong interaction between rGO template and the MoS_2 nanoparticles. Based on all above characterizations, we can conclude that the 3D printed materials form a highly porous MoS_2-rGO aerogels after thermal treatment, with small MoS_2 nanoparticles strongly anchored on the framework of thin stack of rGO sheets as illustrated in Fig. 8c.

Thermogravimetric analysis (TGA) was carried out to determine the mass composition of the MoS_2-rGO aerogels. The mass loss was measured from room temperature to 650 °C in air. As shown in Fig. 8d, bare rGO (blue) remained stable below 350 °C and then slowly lost 10% of the mass up to ~480 °C. The mass rapidly dropped above 480 °C and reach a steady level of 12% after 550 °C, likely in form of residual graphitized carbon. Bare MoS_2 (red) was oxidized to MoO_3 as illustrated by the 7% mass drop after 500 °C. The MoS_2-rGO aerogel (black) behaved as a combination of the above two components. The mass percentage of MoS_2 was measured to be 78% at the temperature above 600 °C. Based on these TGA data, the total weight percentage of the MoS_2-rGO aerogel at 650 °C in air can be expressed as:

$$(\text{Total Weight})\% = ((\text{Weight}\%)_{MoS2} \times 93\%) + ((\text{Weight}\%)_{rGO} \times 12\%) \quad (1)$$

$$78\% = ((\text{Weight}\%)_{MoS2} \times 93\%) + ((1-(\text{Weight}\%)_{MoS2}) \times 12\%) \quad (2)$$

Thus, the mass percentage of MoS_2 in the MoS_2-rGO aerogels can be calculated to be 81.5%. This value is used in calculating the specific capacity of Na^+ storage in later sections.

SIBs have been at the forefront of recent energy storage research since the high cost of lithium precursors makes LIBs unsustainable for large-scale applications such as grid-storage backup [27,28]. SIBs can replace Li^+ ions with more abundant Na^+ ions which have very similar chemical properties. But this encounters a challenge since few materials can serve as stable intercalation host for the large Na^+ ions (with an ionic radius of 0.102 nm vs 0.076 nm for Li) [6,7]. Recently MoS_2 has been recognized as an attractive electrode material for SIBs owing to its suitable layered structure for Na^+ intercalation [29–34]. However, the low intrinsic electrical conductivity hinders its ability as a standalone electrode material. Numerous efforts have been made to combine carbon based materials with MoS_2 to form composites for better performance [12,19,20,35–42]. We envision that the highly porous 3D printed MoS_2-rGO hybrid structure may be an effective way to fully use the Na^+ ion storage capability of MoS_2 and 3D printing for fabrication of complex-structures, which may find broad applications in energy storage devices.

The Na-ion storage properties of the 3D printed MoS_2-rGO aerogels on nickel foam in the half-cell configuration using CR2032 coin cells are shown in Fig. 9. The insertion and extraction specific capacities from the sequential galvanostatic charge-discharge tests at five constant current densities ranging from 100 to 1000 mA/g are shown in Fig. 9a. Ten complete charge-discharge cycles have been applied at each current rate. In the initial 10 cycles at 100 mA/g current density, the insertion capacity rapidly drops from about 800 mAh/g (in the 1st cycle) to 429 mAh/g (in the 10th cycle). Such initial instability is commonly observed in SIB materials [12,38]. This value drops to 334, 284, 236 and 189 mAh/g as the current density is raised to 250, 500, 750 and 1000 mA/g at the 11th, 21st, 31st and 41st cycles, respectively. The cell becomes more stable in later high-current cycles. At the 51st cycle, the previous charge-discharge sequence is repeated. While the specific capacity slightly drops in the 2nd sequence, to 277 mAh/g (at 100 mA/g in the 51st cycle), 193 mAh/g (at 250 mA/g in the 61st cycle), 169 mAh/g (at 500 mA/g in the 71st cycle), 139 mAh/g (at 750 mA/g in the 81st cycle) and 122 mAh/g (at 1000 mA/g in the 91st cycle), respectively, it is noteworthy that the capacity values remain almost constant at high charge-discharge rates from the 71st to 100th cycles.

The corresponding specific capacity during extraction is somewhat lower than the insertion processes. The difference is substantial in the initial 10 cycles at the lowest current density of 100 mA/g but quickly decreases in later cycles, particularly at higher current densities. In the second-rate sequence from the 51st to 100th cycles, the difference

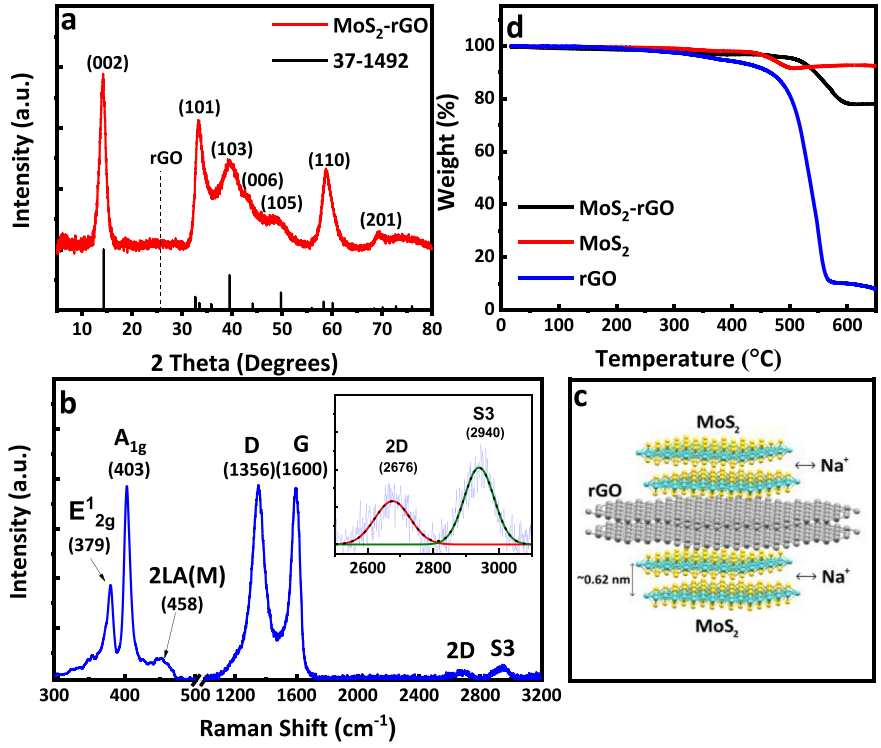

Fig. 8. a) XRD pattern and b) Raman spectrum of 3D printed MoS_2-rGO aerogels. The inset in panel b shows the enlarged region of the Raman spectrum. c) An atomic model to illustrate the stack of MoS_2 layers on the rGO template. d) Thermogravimetric analysis of the MoS_2-rGO aerogel, pure MoS_2 nanoparticles and pure rGO nanosheets. The measurements were done in air from room temperature to 650 °C. (For interpretation of the references to color in this figure, the reader is referred to the web version of this article.)

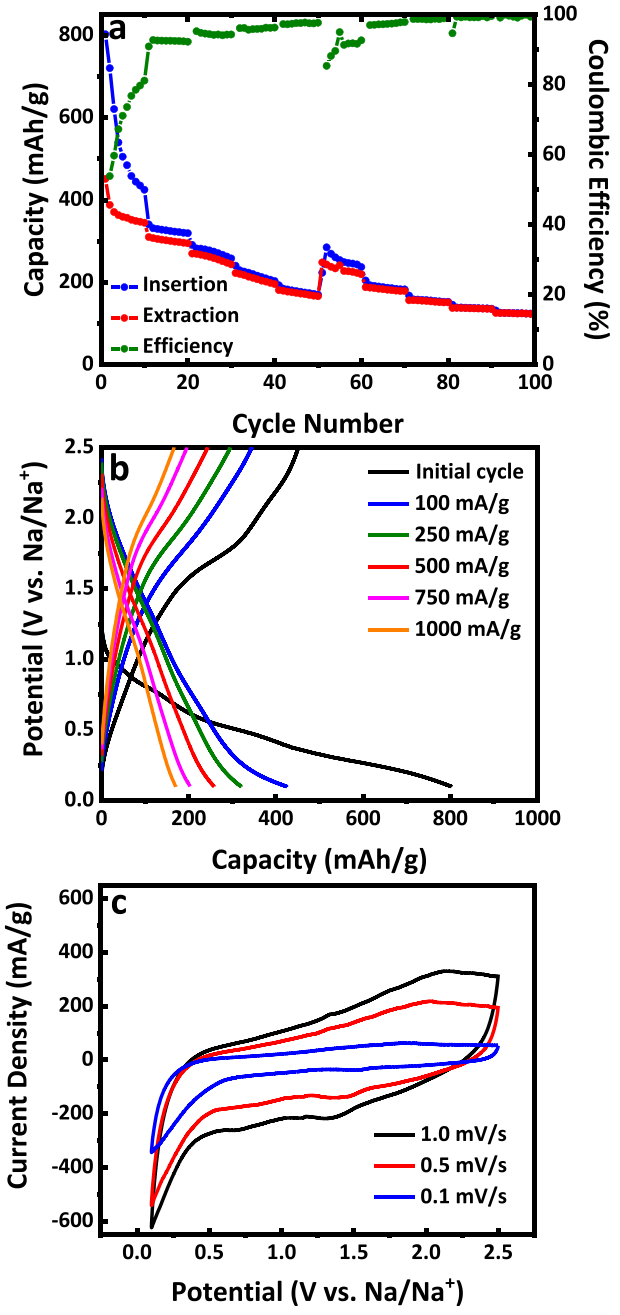

Fig. 9. Electrochemical characterization of the MoS_2-rGO aerogel. a) Rate performance at 5 different current density values (100, 250, 500, 750, and 1000 mA/g), each for 10 charge-discharge cycles in the potential range of 2.5–0.1 V (vs Na/Na^+). b) The galvanostatic charge-discharge curves of the first cycle at 100 mA/g in comparison with those in the 10th cycle at the current density values (100, 250, 500, 750, and 1000 mA/g) in the rate-performance test shown in (a). c) Cyclic voltammetry curves at the scan rate of 0.1, 0.5 and 1.0 mV/s in the potential range of 2.5–0.1 V (vs Na/Na^+).

between the insertion and extraction cycles becomes negligible except at the lowest current density of 100 mA/g. Another way to view this is by the columbic efficiency which is calculated as the percentage ratio of the Na^+ extraction capacity to the Na^+ insertion capacity of the prior step, as shown in the right axis of Fig. 9a. After conditioning the cell in the first 50 cycles at varied current densities, the cell attains >97% columbic efficiency in later cycles when the current density was above 250 mA/g. Even at the lowest current density of 100 mA/g, the columbic efficiency is above 91%.

The representative charge-discharge curves at the last cycles of each current density in the first-rate performance sequence (cycles 1–50) are shown in Fig. 9b in comparison with those in the 1st cycles. The potential decreases as Na^+ ions are inserted in the MoS_2-rGO aerogel electrode and increases as Na^+ ions are extracted. The low columbic efficiency (~52%) in the first cycle is mainly attributed to the long slope at the potential below 0.5 V (vs. Na/Na^+). In stabilized cycles, the potential rises quickly in both charge and discharge processes, giving the steep curves with small bendings at ~1.7 V (for extraction) and ~0.7 V (for insertion). At higher current densities, it becomes closer to smooth tilt lines. These features, particularly the first Na^+ insertion curve, are quite different from the long horizontal plateaus observed in charge-discharge curves with exfoliated bulk MoS_2 materials [12,38]. Such smooth tilt curves are more like the behavior of pseudocapacitors rather than typical batteries. Consistent with the charge-discharge curves, the cyclic voltammograms (CV) in Fig. 9c are dominated by the smooth pseudocapacitor features with only a pair of broad, weak redox waves superimposed on the high capacitive baseline current. A main factor for such pseudocapacitor behavior could be the formation of small (10–50 nm) MoS_2 nanoparticles anchored on the rGO framework. This induces a high magnitude of surface reaction exceeding the bulk intercalation, which is known to generate pseudocapacitive features. Since the surface reaction are much faster, the electrodes tended to be more stable at higher charge-discharge rates and were able to present rather high capacity (~189 mAh/g) at the highest current rate of 1000 mA/g in 41–50th cycles. The highly conductive rGO framework provides the fast electron transport to facilitate such fast surface reactions of the MoS_2 nanoparticles.

It has been well established that the Na^+ insertion mechanism in MoS_2 involves a two-step process, i.e. reversible Na^+ intercalation to form Na_xMoS_2 (up to $x = 2$) followed by an irreversible conversion reaction to form Mo metal and sodium sulfide, as illustrated in Eqs. (3) and (4) [38]:

$$MoS_2 + xNa^+ + xe^- \rightarrow Na_xMoS_2 \ (\text{with } x \le 2) \quad (3)$$

$$Na_xMoS_2 + (4 - x)\ Na^+ + (4 - x)e^- \rightarrow 2Na_2S + Mo (\text{with } 2 \le x \le 4) \quad (4)$$

The theoretical capacity following Eq. (3) is 334 mAh/g which can be expanded up to 667 mAh/g if reaction (4) is involved. To avoid the irreversible degradation, the low potential limit in our battery tests (as shown in Fig. 9) was set at 0.10 V (vs Na/Na^+) even though substantially higher specific capacity can be obtained with lower potential setting, such as 0.01 or 0.005 V (vs Na/Na^+) in literature [12,38,39]. Referring to the theoretical capacity of 334 mAh/g, the C-rates in the rate-

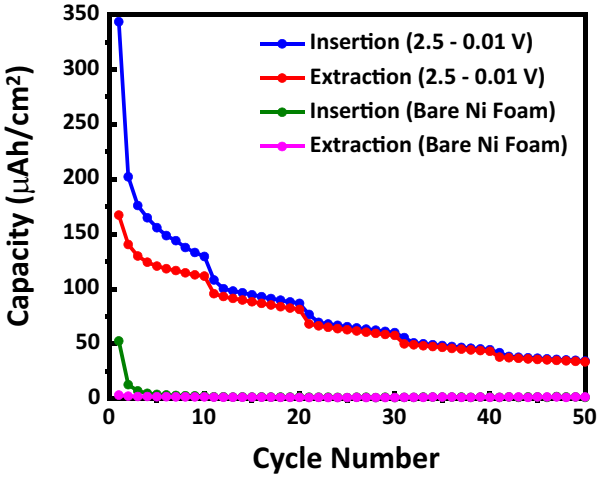

Fig. 10. Comparison of the galvanostatic charge-discharge rate performance of a bare nickel foam with the MoS_2-rGO aerogel in a Ni foam at current rates of 100, 250, 500, 750 and 1000 mA/g.

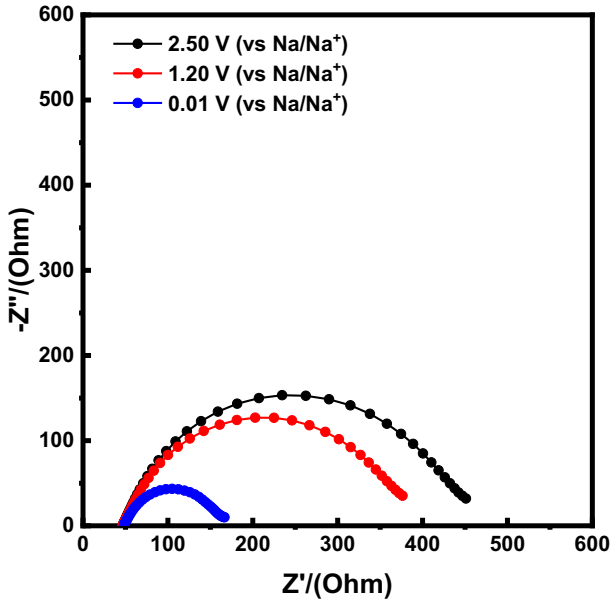

Fig. 11. Nyquist plots of the electrochemical impedance spectra of the 3D printed MoS_2-rGO aerogel electrode in the frequency range of 100 kHz to 10 Hz at different electrode potentials.

performance tests in Fig. 9 are about C/3.3 (100 mA/g), C/1.3 (250 mA/g), 1.5C (500 mA/g), 2.25C (750 mA/g) and 3C (1000 mA/g).

The specific capacity in the initial 10 cycles at C/3.3 rate are ~800 to 429 mAh/g, clearly above the theoretical capacity of 334 mAh/g based on Eq. (3). Control experiments have been carried out to understand this. Fig. 10 shows that sodium plating or other side reactions on Ni foam are negligible. Hence it is likely that the conversion reaction following Eq. (4) occurred. It has been reported that this could happen at the potential below 0.4 V (vs Na/Na^+) [38]. This irreversible reaction is likely much slower than Na^+ intercalation. As a result, its contribution is more evident at the low C-rates. Another possibility of the extra capacity may be due to Na^+ ion intercalation into the rGO framework. Interestingly, the electrochemical impedance spectroscopy (EIS) measurements show that the charge transfer resistance R_{ct} (the real impedance value represented by the diameter of the semicircles in Nyquist plot in Fig. 11) decreases from 400 to 120 Ω as the electrode potential is reduced from 2.50 V to 0.01 V. This trend indicates that reduction of MoS_2 into metallic Mo by Eq. (4), rather than Na^+ intercalation into rGO, is the dominant mechanism for the high capacity at low C-rates. The trend of R_{ct} versus potential is also opposite to the report by Sahu et al. [38] who observed an increased R_{ct} at lower potential due to formation of thicker solid electrolyte interphase (SEI) on the MoS_2 surface. The 3D printed MoS_2-rGO aerogel electrode was able to reduce the SEI formation. Reversible charge-discharge profiles and good electrode stability can be obtained by implementing C/1.3 or higher C-rates. It is noteworthy that the specific capacity of 193 mAh/g and columbic efficiency of 97% at 250 mA/g (i.e. C/1.3) after the electrode was stabilized in cycles 61–70 are promising metrics for future SIBs. Higher C-rates (>1.5 C) yielded even better columbic efficiency over 99%.

More control experiments have been carried out to support of the advantages of the 3D printed porous MoS_2-rGO aerogel structure. Fig. 12 illustrates that direct printing MoS_2-rGO aerogel on a planar copper foil can improve the stability and columbic efficiency at the lowest current density (100 mA/g). But the capacity quickly faded as the C-rate is increased, which is mainly due to the poor adhesion and high resistance at the interface of MoS_2-rGO aerogel and Cu surface. Fig. 13 shows that the conventional thin-film electrode made by the composite consisting of MoS_2 powder mixed with carbon black and polyvinylidene fluoride binder (at 70:20:10 weight ratio) also show better stability and columbic efficiency at the lowest current density (100 mA/g). However, the specific capacity is below 200 mAh/g, significantly lower than that of the 3D printed MoS_2-rGO aerogel in Ni foam (~429 to 800 mAh/g). Particularly, the 3D printed MoS_2-rGO aerogel in Ni foam is far better than the conventional electrodes at the current density above 250 mA/g. Interestingly, even though the MoS_2 nanoparticle size is larger (>200 nm) in the composite electrode, it is still behaved as pseudocapacitors. Clear battery-like redox waves were only observed by CV in the first two cycles. The Na^+ intercalation may have quickly disrupt the MoS_2 crystal structure and break it into smaller nanoparticles in these cycles.

3. Conclusion

The MoS_2-rGO aerogel has been successfully printed by a 3D freeze-printing method, which integrates inkjet printing and freeze casting to provide the capability to control microstructure of hybrid materials in addition to the macroscopic architectures. A MoS_2 precursor (ammonium thiomolybdate) mixed with single layer graphene oxide sheets is used as the ink. The post-treatments by freeze-drying and thermal annealing are able to convert the MoS_2 precursor and GO into a hybrid structure consisting of MoS_2 nanoparticles anchored on the surface of a highly porous rGO framework. The interconnected graphene network in such 3D aerogels has been found to effectively enhance the electrical conductivity and mechanical strength while the large pores (~3–5 μm) facilitate the fast ion transport. The electrical energy storage capability of this porous MoS_2-rGO aerogel has been demonstrated as an anode for sodium ion batteries. In the initial 10 cycles, it shows a high specific

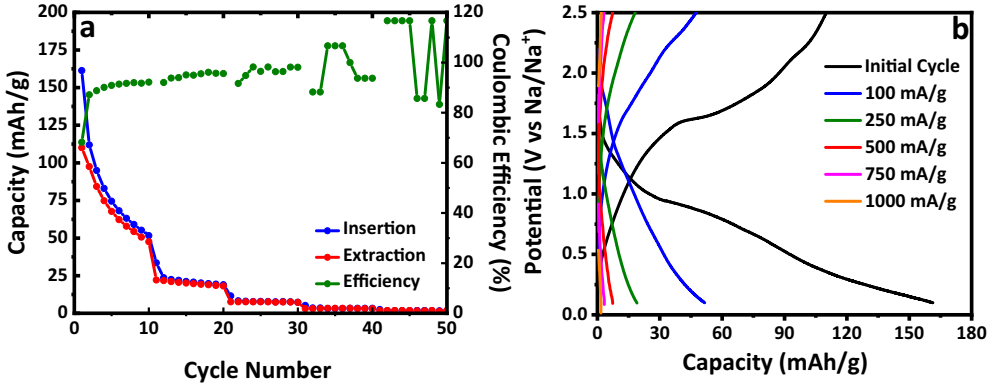

Fig. 12. Electrochemical characterization of the MoS_2-rGO aerogel printed on a planar copper foil. a) Rate performance at 5 different current density values (100, 250, 500, 750, and 1000 mA/g), each for 10 charge-discharge cycles in the potential range of 2.5–0.1 V (vs Na/Na^+). b) Galvanostatic charge-discharge profiles of the initial (black) and the last cycle at current density of 100 (blue), 250 (green), 500 (red), 750 (magenta) and 1000 (orange) mA/g in the rate performance. (For interpretation of the references to color in this figure legend, the reader is referred to the web version of this article.)

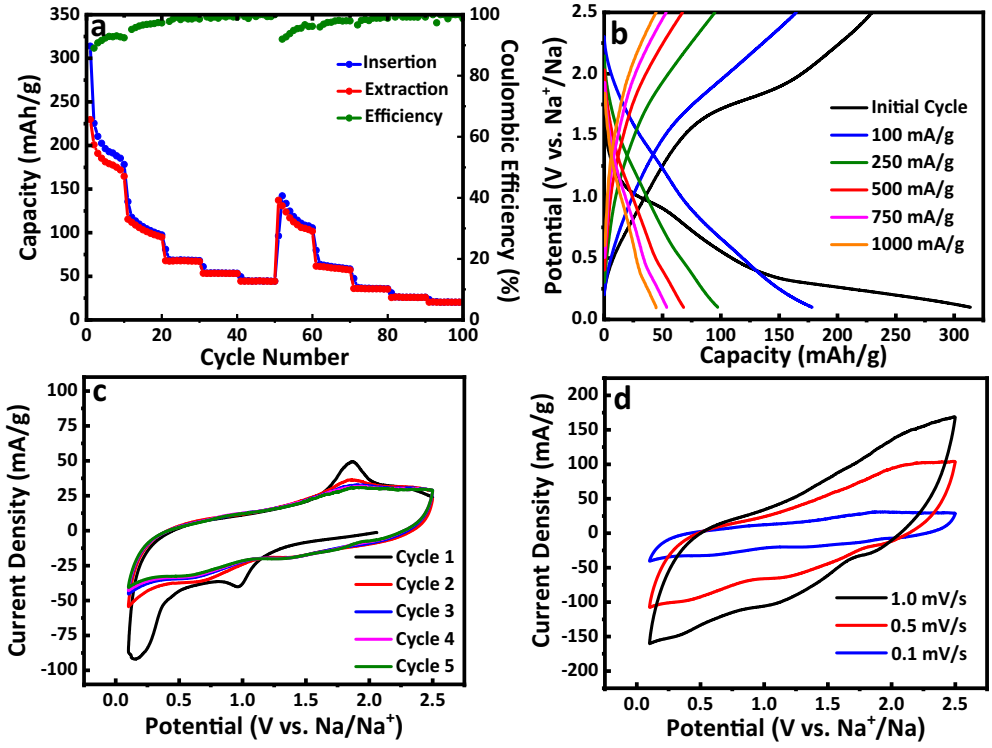

Fig. 13. Electrochemical characterization of the MoS_2 powder mixed with carbon black additive and polyvinylidene difluoride binder (70/20/10 weight ratio) on a copper foil in the potential range of 2.5–0.1 V (vs Na/Na^+). a) Rate performance at 5 different current density values (100, 250, 500, 750, and 1000 mA/g), each for 10 charge-discharge cycles. b) Galvanostatic charge-discharge profiles of the initial (black) and last cycle at current density of 100 (blue), 250 (green), 500 (red), and 750 (magenta) and 1000 (orange) mA/g in the rate performance. Cyclic voltammetry curves of c) the first five cycles at a scan rate of 0.1 mV/s and d) later cycles at 0.1 (blue), 0.5 (red) and 1.0 (black) mV/s. (For interpretation of the references to color in this figure legend, the reader is referred to the web version of this article.)

capacity changing from ~800 to 429 mAh/g at 100 mA/g (~C/3.3 rate), which involves both reversible 2 Na^+ insertion and irreversible conversion of MoS_2 into metallic Mo. At higher rates in later cycles, the conversion reaction is substantially reduced, showing significantly improved stability that is dominated by fast pseudocapacitive surface reactions of Na^+ ion with MoS_2 nanoparticles. This study demonstrates the potential to use 3D printing technology to fabricate the macroporous electrode materials that can sustain high-capacity intercalation of large Na^+ ions, which opens a new direction of 3D printing for energy storage applications.

4. Experiment

Ammonium thiomolybdate (ATM) and graphene oxide (GO) were purchased from Sigma Aldrich (St. Louis, MO, USA) and Cheap Tubes (Cambridgeport, VT, USA), respectively. In typical experiments, 72 mg ATM and 20 mg GO were dispersed into 2 mL water to form a viscous precursor ink for 3D drop-on-demand (DOD) ink jet printing. ATM-GO ink droplets were deposited onto a 0.65 mm thick (1.6 mm unpressed) nickel foam (MTI Corporation, Richmond, CA) with Microfab inkjet printing setup (Plano, TX). The temperature of the Ni foam was preset to −30 °C with a cold plate. The printing was programmed at a specific flow rate and moved following a designed path (at eject voltage of 80 V, frequency of 100 Hz, and travelling velocity of 60 mm/s). The deposited ink droplets infiltrated into the large holes in the Ni foam and rapidly froze into solids, with water turning into small ice crystals in the composite. The 3D printed ATM-GO composites were then placed in a freezer set at −70 °C for 24 h to achieve further ice crystal growth followed by sublimation (−50 °C for 48 h) to remove the water and form an intermediate aerogel structure. The intermediate aerogels (red-brown color) were thermally annealed in 3% hydrogen (97% argon) for 2 h at 600 °C to convert the ATM precursor into black MoS_2-rGO aerogels.

The morphology of the MoS_2-rGO aerogels was investigated using a Versa 3D Dual Beam (FEI, Hillsboro, OR) field emission scanning electron microscope (SEM). The microstructure of the sample was examined using a Tecnai F20 XT (FEI, Hillsboro, OR) high resolution transmission electron microscope (HRTEM). The crystallinity was evaluated using a PANalytical Empyrean (PANalytical, Almelo, The Netherlands) x-ray diffractometer (XRD). Diffraction analysis was conducted from 10° to 60° using a Cu K_α source (8979 eV). Raman spectra were obtained using a Renishaw inVia confocal Raman microscope (Gloucestershire, UK) at a laser wavelength of 532 nm. Thermal gravimetric analyses were carried out with a TA Instrument Q50 (New Castle, DE) from room temperature to 650 °C.

To evaluate electrochemical performance, the MoS_2-rGO electrode was assembled against a 16-mm dia. sodium disk anode in a stainless steel coin cell (CR2032, MTI Corporation, Richmond, CA). A 0.65 mm thick glass fiber disk (El-Cell, Hamburg, Germany) was used as the separator. The cell was assembled in an argon filled M-Braun LabStar50 stainless steel glovebox (Garching, Germany) with <1 ppm of O_2 and H_2O contents. The electrolyte consisted of 1.0 M sodium perchlorate ($NaClO_4$) in propylene carbonate (PC). Galvanostatic charge-discharge cycles were performed using a 8-channel battery analyzer (MTI Corporation, Richmond, CA). All gravimetric capacities were calculated relative to the mass of MoS_2. Cyclic voltammetry (CV) measurements and electrochemical impedance spectroscopy (EIS) were performed using a CHI760D potentiostat (CH Instruments, Austin, TX).

CRediT authorship contribution statement

Emery Brown: Conceptualization, Data curation, Formal analysis, Investigation, Methodology, Validation, Visualization, Writing - original draft, Writing - review & editing. **Pengli Yan:** Conceptualization, Data curation, Formal analysis, Investigation, Methodology, Validation, Visualization, Writing - original draft, Writing - review & editing. **Halil Tekik:** Formal

analysis, Software, Writing - review & editing. **Ayyappan Elangovan:** Formal analysis, Software, Writing - review & editing. **Jian Wang:** Data curation, Formal analysis, Investigation, Writing - review & editing. **Dong Lin:** Conceptualization, Formal analysis, Funding acquisition, Project administration, Resources, Writing - review & editing. **Jun Li:** Conceptualization, Formal analysis, Funding acquisition, Project administration, Resources, Writing - review & editing.

Acknowledgments

We would like to thank Jacob Hughes and Brice Lacroix at Kansas State University (KSU) for the Raman spectroscopy analysis, Shah Valloppilly at the University of Nebraska Center for Materials and Nanoscience (NCMN), Colleen Gura and Ian Andree at KSU for XRD analysis, Xingzhang Li and Anand Sarella at NCMN for TEM imaging, and Dan Boyle of KSU for helping with SEM imaging. We would also like to give special thanks to Manomi Perera, Chamara Gunawardana, and Christer Aakeröy of KSU for their help in the TG analysis. The materials characterization in this work was partially supported by a National Science Foundation (NSF) grant CBET-1703263 and the battery tests and personnel (JL and JEB) were supported by NSF grant DMR-1707585. We would also like to thank the support from the NSF under Award No. OIA-1656006 and matching support from the State of Kansas through the Kansas Board of Regents and the support from Johnson Cancer Center.

References

[1] S. Ke, W. Teng-Sing, A.B. Yeop, S.J. Yoon, D.S. J., L.J. A., 3D printing of interdigitated Li-ion microbattery architectures, Adv. Mater. 25 (33) (2013) 4539–4543.
[2] K. Fu, Y. Wang, C. Yan, Y. Yao, Y. Chen, J. Dai, S. Lacey, Y. Wang, J. Wan, T. Li, Z. Wang, Y. Xu, L. Hu, Graphene oxide-based electrode inks for 3D-printed lithium-ion batteries, Adv. Mater. 28 (13) (2016) 2587–2594.
[3] C.W. Foster, M.P. Down, Y. Zhang, X. Ji, S.J. Rowley-Neale, G.C. Smith, P.J. Kelly, C.E. Banks, 3D printed graphene based energy storage devices, Sci. Rep. 7 (2017) 42233.
[4] J. Hu, Y. Jiang, S. Cui, Y. Duan, T. Liu, H. Guo, L. Lin, Y. Lin, J. Zheng, K. Amine, F. Pan, 3D-printed cathodes of $LiMn_{1-x}Fe_xPO_4$ nanocrystals achieve both ultrahigh rate and high capacity for advanced Lithium-ion battery, Adv. Energy Mater. 6 (18) (2016) 1600856.
[5] V.G. Rocha, E. García-Tuñón, C. Botas, F. Markoulidis, E. Feilden, E. D'Elia, N. Ni, M. Shaffer, E. Saiz, Multimaterial 3D printing of graphene-based electrodes for electrochemical energy storage using thermoresponsive inks, ACS Appl. Mater. Interfaces 9 (42) (2017) 37136–37145.
[6] K. Zhu, C. Zhang, S. Guo, H. Yu, K. Liao, G. Chen, Y. Wei, H. Zhou, Sponge-like cathode material self-assembled from two-dimensional V_2O_5 nanosheets for sodium-ion batteries, ChemElectroChem 2 (11) (2015) 1660–1664.
[7] G.-L. Xu, R. Amine, A. Abouimrane, H. Che, M. Dahbi, Z.-F. Ma, I. Saadoune, J. Alami, W.L. Mattis, F. Pan, Z. Chen, K. Amine, Challenges in developing electrodes, electrolytes, and diagnostics tools to understand and advance sodium-ion batteries, Adv. Energy Mater. 1702403 (2018).
[8] M.A. Worsley, S.J. Shin, M.D. Merrill, J. Lenhardt, A.J. Nelson, L.Y. Woo, A.E. Gash, T.F. Baumann, C.A. Orme, Ultralow density, monolithic WS_2, MoS_2, and MoS_2/graphene aerogels, ACS Nano 9 (5) (2015) 4698–4705.
[9] J. Wang, J. Liu, D. Chao, J. Yan, J. Lin, Z.X. Shen, Self-assembly of honeycomb-like MoS_2 nanoarchitectures anchored into graphene foam for enhanced lithium-ion storage, Adv. Mater. 26 (42) (2014) 7162–7169.
[10] Y. Wang, D. Chen, X. Yin, P. Xu, F. Wu, M. He, Hybrid of MoS_2 and reduced graphene oxide: a lightweight and broadband electromagnetic wave absorber, ACS Appl. Mater. Interfaces 7 (47) (2015) 26226–26234.
[11] X. Xu, Y. Sun, W. Qiao, X. Zhang, X. Chen, X. Song, L. Wu, W. Zhong, Y. Du, 3D MoS_2-graphene hybrid aerogels as catalyst for enhanced efficient hydrogen evolution, Appl. Surf. Sci. 396 (2017) 1520–1527.
[12] L. David, R. Bhandavat, G. Singh, MoS2/graphene composite paper for sodium-ion battery electrodes, ACS Nano 8 (2) (2014) 1759–1770.
[13] F.K. Perkins, A.L. Friedman, E. Cobas, P.M. Campbell, G.G. Jernigan, B.T. Jonker, Chemical vapor sensing with monolayer MoS_2, Nano Lett. 13 (2) (2013) 668–673.
[14] Q. Zhang, F. Zhang, S.P. Medarametla, H. Li, C. Zhou, D. Lin, 3D printing of graphene aerogels, Small 12 (13) (2016) 1702–1708.
[15] G. Zhao, C. Zhou, D. Lin, Tool path planning for directional freezing-based three-dimensional printing of nanomaterials, J. Micro Nano-Manuf. 6 (1) (2017) (010905-010905-5).
[16] Y. Pengli, B. Emery, S. Qing, L. Jun, W. Jian, X. Changxue, Z. Chi, L. Dong, Metallic aerogels: 3D printing hierarchical silver nanowire aerogel with highly compressive resilience and tensile elongation through tunable Poisson's ratio (small 38/2017), Small 13 (38) (2017).
[17] G. Zhao, D. Lin, C. Zhou, Thermal analysis of directional freezing based graphene aerogel three-dimensional printing process, J. Micro Nano-Manuf. 5 (1) (2017), 011006.
[18] V.C.-F. Li, C.K. Dunn, Z. Zhang, Y. Deng, H.J. Qi, Direct ink write (DIW) 3D printed cellulose nanocrystal aerogel structures, Sci. Rep. 7 (1) (2017) 8018.
[19] X. Xie, Z. Ao, D. Su, J. Zhang, G. Wang, MoS_2/graphene composite anodes with enhanced performance for sodium-ion batteries: the role of the two-dimensional heterointerface, Adv. Funct. Mater. 25 (9) (2015) 1393–1403.
[20] Y.-X. Wang, S.-L. Chou, D. Wexler, H.-K. Liu, S.-X. Dou, High-performance sodium-ion batteries and sodium-ion pseudocapacitors based on MoS_2/graphene composites, Chem. Eur. J. 20 (31) (2014) 9607–9612.
[21] P.A. Bertrand, Surface-phonon dispersion of MoS_2, Phys. Rev. B 44 (11) (1991) 5745–5749.
[22] C. Lee, H. Yan, L.E. Brus, T.F. Heinz, J. Hone, S. Ryu, Anomalous lattice vibrations of single- and few-layer MoS_2, ACS Nano 4 (5) (2010) 2695–2700.
[23] J.M. Chen, C.S. Wang, Second order Raman spectrum of MoS_2, Solid State Commun. 14 (9) (1974) 857–860.
[24] B.C. Windom, W.G. Sawyer, D.W. Hahn, A Raman spectroscopic study of MoS_2 and MoO_3: applications to tribological systems, Tribol. Lett. 42 (3) (2011) 301–310.
[25] G.L. Frey, R. Tenne, M.J. Matthews, M.S. Dresselhaus, G. Dresselhaus, Raman and resonance Raman investigation of MoS_2 nanoparticles, Phys. Rev. B 60 (4) (1999) 2883–2892.
[26] H. Wang, J.T. Robinson, X. Li, H. Dai, Solvothermal reduction of chemically exfoliated graphene sheets, J. Am. Chem. Soc. 131 (29) (2009) 9910–9911.
[27] J.-M. Tarascon, Is lithium the new gold? Nat. Chem. 2 (2010) 510.
[28] M.D. Slater, D. Kim, E. Lee, C.S. Johnson, Sodium-ion batteries, Adv. Funct. Mater. 23 (8) (2013) 947–958.
[29] W.-H. Ryu, J.-W. Jung, K. Park, S.-J. Kim, I.-D. Kim, Vine-like MoS_2 anode materials self-assembled from 1-D nanofibers for high capacity sodium rechargeable batteries, Nanoscale 6 (19) (2014) 10975–10981.
[30] M. Xu, F. Yi, Y. Niu, J. Xie, J. Hou, S. Liu, W. Hu, Y. Li, C.M. Li, Solvent-mediated directionally self-assembling MoS_2 nanosheets into a novel worm-like structure and its application in sodium batteries, J. Mater. Chem. A 3 (18) (2015) 9932–9937.
[31] Z. Hu, L. Wang, K. Zhang, J. Wang, F. Cheng, Z. Tao, J. Chen, MoS_2 nanoflowers with expanded interlayers as high-performance anodes for sodium-ion batteries, Angew. Chem. 126 (47) (2014) 13008–13012.
[32] D. Su, S. Dou, G. Wang, Ultrathin MoS_2 nanosheets as anode materials for sodium-ion batteries with superior performance, Adv. Energy Mater. 5 (6) (2015) (1401205-n/a).
[33] G.S. Bang, K.W. Nam, J.Y. Kim, J. Shin, J.W. Choi, S.-Y. Choi, Effective liquid-phase exfoliation and sodium ion battery application of MoS_2 nanosheets, ACS Appl. Mater. Interfaces 6 (10) (2014) 7084–7089.
[34] X. Wang, Y. Li, Z. Guan, Z. Wang, L. Chen, Micro-MoS_2 with excellent reversible sodium-ion storage, Chem. Eur. J. 21 (17) (2015) 6465–6468.
[35] S. Zhang, X. Yu, H. Yu, Y. Chen, P. Gao, C. Li, C. Zhu, Growth of ultrathin MoS_2 nanosheets with expanded spacing of (002) plane on carbon nanotubes for high-performance sodium-ion battery anodes, ACS Appl. Mater. Interfaces 6 (24) (2014) 21880–21885.
[36] S.H. Choi, Y.N. Ko, J.-K. Lee, Y.C. Kang, 3D MoS_2–graphene microspheres consisting of multiple nanospheres with superior sodium ion storage properties, Adv. Funct. Mater. 25 (12) (2015) 1780–1788.
[37] C. Zhu, X. Mu, P.A. van Aken, Y. Yu, J. Maier, Single-layered ultrasmall nanoplates of MoS_2 embedded in carbon nanofibers with excellent electrochemical performance for lithium and sodium storage, Angew. Chem. Int. Ed. 53 (8) (2014) 2152–2156.
[38] T.S. Sahu, S. Mitra, Exfoliated MoS_2 sheets and reduced graphene oxide-an excellent and fast anode for sodium-ion battery, Sci. Rep. 5 (2015) 12571.
[39] J. Wang, C. Luo, T. Gao, A. Langrock, A.C. Mignerey, C. Wang, An advanced MoS_2/carbon anode for high-performance sodium-ion batteries, Small 11 (4) (2015) 473–481.
[40] W. Qin, T. Chen, L. Pan, L. Niu, B. Hu, D. Li, J. Li, Z. Sun, MoS_2-reduced graphene oxide composites via microwave assisted synthesis for sodium ion battery anode with improved capacity and cycling performance, Electrochim. Acta 153 (2015) 55–61.
[41] L. Jiang, B. Lin, X. Li, X. Song, H. Xia, L. Li, H. Zeng, Monolayer MoS_2—graphene hybrid aerogels with controllable porosity for lithium-ion batteries with high reversible capacity, ACS Appl. Mater. Interfaces 8 (2016) 2680–2687.
[42] J. He, P. Li, W. Lv, K. Wen, Y. Chen, W. Zhang, Y. Li, W. Qin, W. He, Three-dimensional hierarchically structured aerogels constructed with layered MoS_2/graphene nanosheets as free-standing anodes for high-performance lithium ion batteries, Electrochim. Acta 215 (2016) 12–18.